applied sciences

MDPI

Article

TAB Series-Resonant DC-DC Converter and Multi-Phase-Shift Based Global Optimization Modulation

Fengjiang Wu, Kaixuan Wang and Jianyong Su *

Department of Electrical Engineering, Harbin Institute of Technology, Harbin 150001, China; shimeng@hit.edu.cn (F.W.); wangkaixuanhit@163.com (K.W.)
* Correspondence: sujianyong@hit.edu.cn

Abstract: In this paper, a triple-active-bridge resonant dc-dc converter with the ability of topology-level power decoupling is proposed. The power coupling between the two dc ports is eliminated by adding a resonant capacitor to the common port. The operation principle and the steady-state power characteristics are analyzed. On this basis, a multi-phase-shift-based global optimization modulation is proposed to minimize the RMS values of the transformer currents in the entire power and voltage range, thus increasing the global efficiency. An experimental prototype is built to verify the correctness and availability of the proposed power decoupling topology and optimized modulation.

Keywords: three-port converter; power decoupled; power loss; multi-phase-shift modulation

Citation: Wu, F.; Wang, K.; Su, J. TAB Series-Resonant DC-DC Converter and Multi-Phase-Shift Based Global Optimization Modulation. *Appl. Sci.* **2022**, *12*, 6783. https://doi.org/10.3390/app12136783

Academic Editor: Edris Pouresmaeil

Received: 8 June 2022
Accepted: 2 July 2022
Published: 4 July 2022

1. Introduction

Due to the advantages of high power density, competitive low cost, and multi-port interconnection, the three-port isolated dc-dc converter has emerged as an attractive solution to construct future renewable energy systems, such as the micro-grid, hybrid energy storage systems, electrical vehicles, etc. [1–3].

According to the number of transformer winding, the existing isolated three-port dc-dc converters mainly include the single-transformer type and the two-transformer type [4–14]. The single-transformer converter presents a clear advantage regarding the increase of the power density and the system integration. The popular single-transformer three-port converter is the triple-active-bridge (TAB) converter, which consists mainly of two types: inductor-based and resonant-based. For the inductor-type topology, the leakage inductor and external inductor of the transformer winding are used to store energy and transfer power. For the resonant-type topology, resonant tanks are used to transfer power. Combining the principle of this type of converter, the shape of the transformer current of the resonant-type is close to the sinusoidal. The current stress of the resonant-type is significantly lower than that of the inductor-type. Hence, the resonant-type has a better electromagnetic characteristic and low current stress as compared with the inductor-type [15–17]. The resonant-type increases operating efficiency and the utilization rate of the system hardware rated capacity.

The TAB dc-dc converter realizes the galvanic isolation by using the three-winding transformer. The magnetic coupling of the transformer will cause the power coupling among the three ports of the converter. This results in the various ports not being able to transfer power independently and precisely. The existing power decoupling strategies mainly include the topology-level and the control-level ones. In [18], the resonant tanks are added to the TAB converter, then the degree of power coupling is decreased by reducing the proportion of the switching frequency to the resonant frequency. This method cannot completely eliminate power coupling. In addition, the current stress will increase when the resonant frequency is different from the switching frequency. In [19], an isolated three-port converter is proposed. The decoupling resonant tank is added to the battery port, which

results in the power flow between the PV port and dc-bus port being transferred indirectly via the battery port. This increases additional power loss. In [20,21], the decoupling matrix is applied to the control loop to compensate for the coupling between the control variables, then realizes the independent control of the transfer power. The solution of the decoupling matrix depends on the small-signal model of the converter. Thus, the universality of the decoupling network is not very good. Meanwhile, the complexity of the control system is still the challenge of the decoupling strategy at the control level.

Up to now, the single-phase-shift (SPS) modulation is widely used in the TAB converter [22,23]. In SPS modulation, the internal phase-shift angle of the three ports is fixed to 0, only the external phase-shift angle is used to control the magnitude and direction of the transfer power. This modulation is easy to realize. However, there are no other control variables to further optimize the performance of the three-port converter. When the voltage magnitude of the windings of the transformer is not matched, the RMS value and peak value of the transformer current are greatly increased. The power loss becomes much higher and the efficiency is greatly reduced.

The better performance of the converter is realized by increasing the controllable degree of freedom. In a dual-active-bridge converter, the optimization control of the transformer current, reactive power, and power loss is realized by adjusting the relationship between the control variables, thereby improving the operational efficiency of the converter. While the structural coupling of the three-port converter causes the control variables of each port to be interactive. The two equivalent two-port converters are likely to have different optimal operating points of the control variables on the common port when the range of the voltage and transfer power is different. Hence, it is important to propose a unified global optimization modulation based on the multiple controllable variables. It is helpful to reduce power loss and increase efficiency.

In this paper, a topology-level power decoupling TAB converter and its optimized multi-phase-shift modulation are proposed. The innovation and contribution are below. (1) In terms of the topology, a topology-level power decoupling TAB isolated resonant dc-dc converter is proposed in this paper. A resonant capacitor is added to the three-winding transformer to realize the power decoupling at the topology level. The converter realizes the power decoupling only by setting the hardware parameters and without adding an additional controller. Hence, the decoupling effect of the converter is improved and the complexity of the control system is significantly reduced. (2) Meanwhile, different from the inductor-type topology, the energy storage component of the proposed converter is the series-resonant tank, which significantly reduces the current stress and increases the utilization rate of the hardware. (3) In terms of the modulation, the existing TAB converters generally use the single-phase-shift modulation. In this paper, the optimized multi-phase-shift modulation for the TAB converter is proposed. With the increase of the controllable degree of freedom, the performance of the converter is correspondingly improved. On this basis, the RMS value of the transformer current is minimized and the power loss in the entire voltage and power range is accordingly reduced, thus ensuring the high efficiency of the converter.

2. Analysis of Topology and Characteristics

2.1. Topology and Modulation

Figure 1 shows the topology of the proposed isolated TAB resonant dc-dc converter. It contains three H-bridge converters as the basic power conversion unit at each port. The three ports are connected via a three-winding high-frequency transformer and the turn ratio of the transformer is n_1: n_2: n_3. Two resonant tanks are set at port 1 and 2 to temporarily store energy and realize power adjustment. Compared with the standard series-resonant three-port converter, the proposed converter adds a resonant capacitor on port 3 to construct a resonant tank with the leakage inductor L_{k3} of the transformer on port 3. The resonant tank on port 3 is used to realize the power decoupling between port 1 and 2 at the topology level.

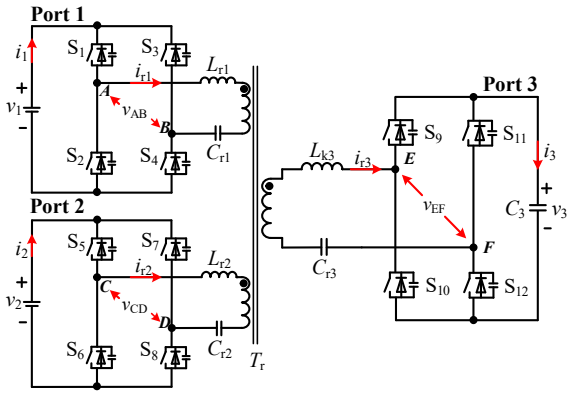

Figure 1. Schematic of the proposed three-port converter.

Port 3 is defined as the common port and it is defined as the forward mode if the power flows into it. The corresponding operation waveforms of the converter under the multi-phase-shift modulation are shown in Figure 2. D_1, D_2, and D_3 represent the internal phase-shift angle of the three ports. The RMS value of the equivalent ac voltage v_{AB}, v_{CD}, and v_{EF} of three ports of the transformer is adjusted by D_1, D_2, and D_3, respectively. φ_{13} represents the external phase-shift angle between port 1 and port 3. φ_{23} represents the external phase-shift angle between port 2 and port 3.

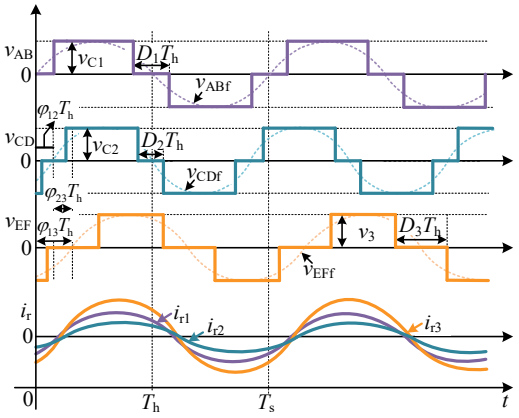

Figure 2. Waveforms of multi-phase-shift modulation for the proposed converter.

For the two-port converter, the triple-phase-shift modulation has been applied and the minimum transformer current is realized by controlling cooperatively the three phase shifts. However, there is the coupling of the two ports on D_3, which causes the optimized modulation in the two-port converter not to be directly applied in the proposed converter.

Next, the power characteristics of the proposed converter are analyzed and then the power decoupling method is proposed. Furthermore, the principle of the multi-phase-shift modulation to minimize the RMS value of the transformer current is analyzed and the process of how to obtain the final relationship among the various phase shifts is derived in detail.

2.2. Power Characteristics Analysis

The power flow analysis in this section adopts the fundamental harmonics approximation (FHA) approach. The variables are normalized to port 3 and represented by " ′ ". $v_{ABf}{}'(t)$, $v_{CDf}{}'(t)$, and v_{EFf} are calculated as

$$v'_{ABf}(t) = \frac{4v_3}{k_1\pi}\cos(\frac{D_1\pi}{2})\sin(\omega_s t + \varphi_{13}\pi) \quad (1)$$

$$v'_{\mathrm{CDf}}(t) = \frac{4v_3}{k_2\pi}\cos(\frac{D_2\pi}{2})\sin(\omega_s t + \varphi_{23}\pi) \tag{2}$$

$$v_{\mathrm{EFf}}(t) = \frac{4v_3}{\pi}\cos(\frac{D_3\pi}{2})\sin(\omega_s t) \tag{3}$$

where $k_1 = n_1v_3/n_3v_1$ is the voltage gain between port 1 and port 3 and $k_2 = n_2v_3/n_3v_2$ is the voltage gain between port 2 and port 3.

Combining the equivalent circuit of the three-winding transformer, the equivalent circuit of the proposed converter is shown in Figure 3a. The impedance of each branch is calculated as

$$\begin{cases} X_{12} = \frac{X'_{r1}X'_{r2}}{X_{r3}} + X'_{r1} + X'_{r2} \\ X_{13} = \frac{X'_{r1}X'_{r3}}{X_{r2}} + X'_{r1} + X'_{r3} \\ X_{23} = \frac{X'_{r2}X'_{r3}}{X_{r1}} + X'_{r2} + X'_{r3} \end{cases} \tag{4}$$

where $X_{\mathrm{r1}}{}'$, $X_{\mathrm{r2}}{}'$ and X_{r3} are the impedance of the resonant tank on port 1, port 2, and port 3, respectively.

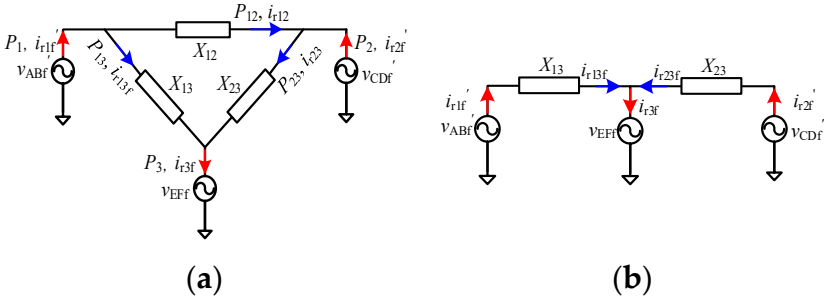

Figure 3. Equivalent circuits of the proposed converter. (**a**) Before power decoupling, (**b**) After power decoupling.

Then, the transformer current of each branch of the equivalent circuit is calculated as

$$i_{\mathrm{r13f}}(t) = \frac{4v_3}{\pi X_{13}}\left[\cos(\frac{D_3\pi}{2})\cos(\omega_s t) - \frac{1}{k_1}\cos(\frac{D_1\pi}{2})\cos(\omega_s t + \varphi_{13}\pi)\right] \tag{5}$$

$$i_{\mathrm{r23f}}(t) = \frac{4v_3}{\pi X_{23}}\left[\cos(\frac{D_3\pi}{2})\cos(\omega_s t) - \frac{1}{k_2}\cos(\frac{D_2\pi}{2})\cos(\omega_s t + \varphi_{23}\pi)\right] \tag{6}$$

$$i_{\mathrm{r12f}}(t) = \frac{4v_3}{\pi X_{12}}\left[\frac{1}{k_2}\cos(\frac{D_2\pi}{2})\cos(\omega_s t + \varphi_{23}\pi) - \frac{1}{k_1}\cos(\frac{D_1\pi}{2})\cos(\omega_s t + \varphi_{13}\pi)\right] \tag{7}$$

Next, the average transfer power in a switching period is expressed as

$$P_{13} = \frac{8{v_3}^2}{\pi^2 k_1 X_{13}}\cos(\frac{D_1\pi}{2})\cos(\frac{D_3\pi}{2})\sin(\varphi_{13}\pi) \tag{8}$$

$$P_{23} = \frac{8{v_3}^2}{\pi^2 k_2 X_{23}}\cos(\frac{D_2\pi}{2})\cos(\frac{D_3\pi}{2})\sin(\varphi_{23}\pi) \tag{9}$$

$$P_{12} = \frac{8{v_3}^2}{\pi^2 k_1 k_2 X_{12}}\cos(\frac{D_1\pi}{2})\ \cos(\frac{D_2\pi}{2})\sin[(\varphi_{13} - \varphi_{23})\pi] \tag{10}$$

The actual average transfer power and its direction are controlled by combining the relationship between the average transfer power of each branch in a switching period and various phase shifts in (8) and (9). From (10), when $\varphi_{13} \neq \varphi_{23}$, the power P_{12} is transferred between port 1 and port 2. P_{12} is namely the coupled power and is undesired.

2.3. Power Decoupling Method

The coupled power between port 1 and 2 is not desired because it causes the power error. Hence, the power decoupling method is discussed in this section. From (10), the coupled power is related to the circuit parameters and is defined as

$$k_c = \frac{8{v_3}^2}{\pi^2 k_1 k_2 X_{12}} \tag{11}$$

It can be seen that kc is inversely proportional to X_{12} between port 1 and port 2 in the equivalent circuit. As X_{12} increases, kc decreases when $X_{12} = \infty$, $k_c = 0$, and $P_{12} = 0$. Thus, the power decoupling is realized. Furthermore, according to (4), X_{12} is closely related to X_{r3}. When $X_{r3} = 0$, $X_{12} = \infty$ and P_{12} is accordingly equal to zero. X_{r3} is calculated as

$$X_{r3} = \left(\frac{f_s}{f_{r3}} - \frac{f_{r3}}{f_s}\right)\sqrt{\frac{L_{k3}}{C_{r3}}} \tag{12}$$

where f_s is the switching frequency, f_{r3} is the resonant frequency of the resonant tank of port 3.

According to (12), when fs is equal to f_{r3}, $X_{r3} = 0$. Therefore, the power decoupling is realized by setting $f_{r3} = f_s$.

The equivalent circuit after power decoupling is shown in Figure 3b. It can be seen that the proposed power decoupling method eliminates the flow path of the transfer power between port 1 and port 2. More importantly, the proposed method only plugs in a resonant capacitor at the common port. Any additional power decoupling control loop is not needed. Therefore, it is easy to implement and avoid increasing the complexity of the control configuration.

3. Global Optimization of Multiple Phase Shifts to Minimize Ohmic Loss

For the converter, besides realizing the real-time adjustment of the transfer power, one important aspect is to reduce the power loss. In theory, there are five phase shifts that can be used to adjust the transfer power. In this section, reducing the power loss and increasing the operating efficiency in the entire voltage and power range are used as the objective to optimize the multi-phase-shift modulation. In addition, the soft-switching performance is analyzed.

The power loss of the converter mainly includes the switching loss P_{sw}, the conduction loss P_{cond}, the copper loss P_{copp}, the iron loss P_{iron}, and so on. Combined with the theoretical analysis and the distribution diagram of the power loss in [24], both P_{cond} and P_{copp} are positively correlated with the square of the RMS value of the transformer current, thus, they are collectively called the ohmic loss P_{ohm}. P_{ohm} has a high proportion of the total power loss in the entire power range. As the transfer power and the transformer current increase, the proportion of P_{ohm} increases accordingly. Hence, reducing P_{ohm} is effective to improve the converter efficiency.

P_{ohm}, $P_{cond,}$ and P_{copp} are respectively calculated as

$$P_{ohm} = P_{cond} + P_{copp} \tag{13}$$

$$P_{cond} = 4R_{DS1}\left(\frac{I_{r1f,rms}}{\sqrt{2}}\right)^2 + 4R_{DS2}\left(\frac{I_{r2f,rms}}{\sqrt{2}}\right)^2 + 4R_{DS3}\left(\frac{I_{r3f,rms}}{\sqrt{2}}\right)^2 \tag{14}$$

$$P_{copp} = R_{tran1}{I_{r1f,rms}}^2 + R_{tran2}{I_{r2f,rms}}^2 + R_{tran3}{I_{r3f,rms}}^2 \tag{15}$$

where R_{DS1}, $R_{DS2,}$ and R_{DS3} respectively denote the on-state resistance of the power switches of each port. R_{tran1}, $R_{tran2,}$ and R_{tran3} respectively denote the resistance of the transformer windings of each port. $I_{r1f,rms}$, $I_{r2f,rms,}$ and $I_{r3f,rms}$ respectively denote the RMS value of the fundamental component of the transformer current of each port.

From (13)–(15), P_{ohm} is closely related to $I_{r1f,rms}$, $I_{r2f,rms,}$ and $I_{r3f,rms}$. The smaller the RMS value of the transformer current is, the smaller the ohmic loss will be. Therefore, the optimization objective of the modulation is equivalent to minimizing the RMS value of the transformer current.

After the power is decoupled between port 1 and port 2, $i_{r1f} = i_{r13f}$, and $i_{r2f} = i_{r23f}$, hence, combining (6) and (7), $I_{r1f,rms,}$ and $I_{r2f,rms}$ are calculated as

$$I_{r1f,\,rms} = \frac{\sqrt{8}v_3}{\pi X_{13}}\sqrt{\left(\frac{1}{k_1}\cos\left(\frac{D_1\pi}{2}\right)\right)^2 + \left(\cos\left(\frac{D_3\pi}{2}\right)\right)^2 - \frac{2}{k_1}\cos\left(\frac{D_1\pi}{2}\right)\cos\left(\frac{D_3\pi}{2}\right)\cos(\varphi_{13}\pi)} \tag{16}$$

$$I_{r2f,\,rms} = \frac{\sqrt{8}v_3}{\pi X_{23}}\sqrt{\left(\frac{1}{k_2}\cos\left(\frac{D_2\pi}{2}\right)\right)^2 + \left(\cos\left(\frac{D_3\pi}{2}\right)\right)^2 - \frac{2}{k_2}\cos\left(\frac{D_2\pi}{2}\right)\cos\left(\frac{D_3\pi}{2}\right)\cos(\varphi_{23}\pi)} \tag{17}$$

The fundamental component of ir3f is composed of i_{r1f} and i_{r2f}. The relationship of the phasors $\vec{I}_{r1f}$, $\vec{I}_{r2f}$ and $\vec{I}_{r3f}$ of the transformer current i_{r1f}, $i_{r2f,}$ and i_{r3f} is shown in Figure 4, where ε is the phase difference between $\vec{I}_{r1f}$ and $\vec{I}_{r2f}$. $I_{r1f,rms}$, $I_{r2f,rms,}$ and $I_{r3f,rms}$ are the magnitude of the phasors $\vec{I}_{r1f}$, $\vec{I}_{r2f}$ and $\vec{I}_{r3f}$, respectively. Hence, $I_{r3f,rms}$ is calculated as

$$I_{r3f,rms} = \sqrt{\left(\frac{n_1}{n_3}I_{r1f,rms}\right)^2 + \left(\frac{n_2}{n_3}I_{r2f,rms}\right)^2 + \frac{2n_1n_2}{{n_3}^2}I_{r1f,rms}I_{r2f,rms}\cos(\varepsilon\pi)} \tag{18}$$

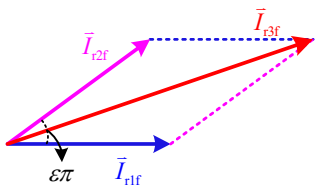

Figure 4. Phasor diagram of the transformer current.

From (18), under the same transfer power, when $I_{r1f,rms,}$ and $I_{r2f,rms}$ are both the minimum, $I_{r3f,rms}$ is also the minimum. Therefore, the functions of the optimization objective are expressed as

$$\begin{aligned} &Minimized\ I_{r1f,\,rms}(D_1,\ D_3,\ \varphi_{13}) \\ &Subject\ to\begin{cases} G_{13}(D_1,\ D_3,\ \varphi_{13}) - {G_{13}}^*({D_1}^*,\ {D_3}^*,\ {\varphi_{13}}^*) = 0 \\ D_1 \in [0,\ 1),\ D_3 \in [0,\ 1),\ \varphi_{13} \in [-0.5,\ 0.5] \end{cases} \end{aligned} \tag{19}$$

$$\begin{aligned} &Minimized\ I_{r2f,\,rms}(D_2,\ D_3,\ \varphi_{23}) \\ &Subject\ to\begin{cases} G_{23}(D_2,\ D_3,\ \varphi_{23}) - {G_{23}}^*({D_2}^*,\ {D_3}^*,\ {\varphi_{23}}^*) = 0 \\ D_2 \in [0,\ 1),\ D_3 \in [0,\ 1),\ \varphi_{23} \in [-0.5,\ 0.5] \end{cases} \end{aligned} \tag{20}$$

where G_{13} and ${G_{13}}^*$, G_{23} and ${G_{23}}^*$ are the index of the actual and desired transfer power of port 1 and port 2, respectively. G_{13} and G_{23} are respectively expressed as

$$G_{13} = \cos\left(\frac{D_1\pi}{2}\right)\cos\left(\frac{D_3\pi}{2}\right)\sin(\varphi_{13}\pi) \tag{21}$$

$$G_{23} = \cos\left(\frac{D_2\pi}{2}\right)\cos\left(\frac{D_3\pi}{2}\right)\sin(\varphi_{23}\pi) \tag{22}$$

Since port 3 is the common port of the two equivalent two-port converter and D_3 is determined by the operating state of both port 1 and port 2, the optimal operating point of

D_3 is analyzed at first. Combining (3), (16), and (17), the average transfer power of port 1 and port 2 are respectively calculated and expressed as

$$P_{13} = \frac{n_1}{n_3} V_{\mathrm{EFf,\,rms}} I_{\mathrm{r1f,rms}} \cos(\theta_1 \pi) = \frac{\sqrt{8} n_1 v_3}{\pi n_3} \cos(\frac{D_3 \pi}{2}) I_{\mathrm{r1f,rms}} \cos(\theta_1 \pi) \tag{23}$$

$$P_{23} = \frac{n_2}{n_3} V_{\mathrm{EFf,\,rms}} I_{\mathrm{r2f,rms}} \cos(\theta_2 \pi) = \frac{\sqrt{8} n_2 v_3}{\pi n_3} \cos(\frac{D_3 \pi}{2}) I_{\mathrm{r2f,rms}} \cos(\theta_2 \pi) \tag{24}$$

where $V_{\mathrm{EFf,rms}}$ is the RMS value of v_{EFf}. θ_1 is the phase difference between v_{EFf} and i_{r1f}. θ_2 is the phase difference between v_{EFf} and i_{r2f}.

From (23) and (24), under the same transfer power, the smaller D_3 is, the smaller $I_{\mathrm{r1f,rms}}$, and $I_{\mathrm{r2f,rms}}$ will be. Therefore, D_3 is always set to 0 under the proposed modulation to minimize the transformer current. On this basis, the KKT conditions based on the Lagrange multiplier method are used to solve the nonlinear optimization problem shown in (19) and (20). According to the range of voltage gain and the transfer power, the optimization results include the following four states and are expressed as (25), (32), (34), and (36).

Furthermore, it is useful to construct the phasor diagram of the fundamental equivalent converter to verify the principle of the optimization strategy in the time domain. The optimization results of the four states and the corresponding phasor diagrams are described as follows.

State 1: when $k_1 < 1$, $k_2 < 1$, ${G_{13}}^* \le \sqrt{1 - {k_1}^2}$ and ${G_{23}}^* \le \sqrt{1 - {k_2}^2}$, the optimization result is expressed as

$$\begin{cases} {D_1}^* = \frac{2}{\pi} \arccos\left(\sqrt{{k_1}^2 + {G_{13}}^{*2}}\right) \\ {D_2}^* = \frac{2}{\pi} \arccos\left(\sqrt{{k_2}^2 + {G_{23}}^{*2}}\right) \\ {\varphi_{13}}^* = \frac{1}{\pi} \arctan(\frac{{G_{13}}^*}{k_1}) \\ {\varphi_{23}}^* = \frac{1}{\pi} \arctan(\frac{{G_{23}}^*}{k_2}) \end{cases} \tag{25}$$

Substituting (25) into (1)–(3), the voltage phasors of the fundamental equivalent converter satisfy

$$\begin{cases} v_{\mathrm{AB}} \cos({\varphi_{13}}^* \pi) = v_{\mathrm{EF}} \\ v_{\mathrm{CD}} \cos({\varphi_{23}}^* \pi) = v_{\mathrm{EF}} \end{cases} \tag{26}$$

Thus, the phasor diagram is shown in Figure 5a. It can be seen that ir1f and ir2f are always in a phase of vEFf in this state. Both the equivalent two-port converters operate at the unity power factor. Hence, the RMS value of the transformer current is the smallest. As the transfer power increases, D_1, D_2, φ_{13} and φ_{23} vary accordingly. It ensures i_{r1f} and i_{r2f} are always in a phase of v_{EFf}, that is, the converter operates at the minimum RMS value of the transformer current. In this state, the per-unit transfer power of port 1 and 2 are simplified and expressed as

$$G_{13} = \cos(\frac{D_1 \pi}{2}) \sin(\varphi_{13} \pi) \tag{27}$$

$$G_{23} = \cos(\frac{D_2 \pi}{2}) \sin(\varphi_{23} \pi) \tag{28}$$

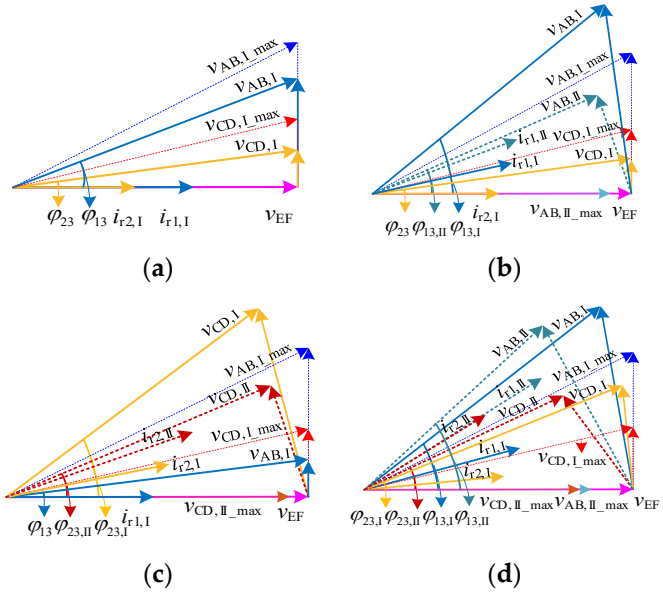

Figure 5. Phasor diagram under proposed modulation. (**a**) State 1, (**b**) State 2, (**c**) State 3, (**d**) State 4.

The soft-switching conditions of this state are analyzed as follows. Combining the analysis of the soft-switching principle in [25], the ZV off is realized naturally. The ZV on is achieved by gating on the in-coming power switch while the anti-parallel diode is conducting. Hence, take port 1 as an example, the ZV-on conditions of the switches are expressed as

$$\begin{cases} i_{r1}(T_h - D_1 T_h/2) > 0 & \text{for } S_1,\ S_3 \\ i_{r1}(D_1 T_h/2) < 0 & \text{for } S_2,\ S_4 \end{cases} \tag{29}$$

Substituting (5) into (29), the ZV-on conditions of the switches on port 1 are expressed as

$$\begin{cases} \cos(\varphi_{13}\pi - D_1\pi/2) > k_1 & \text{for } S_1,\ S_3 \\ \cos(\varphi_{13}\pi + D_1\pi/2) > k_1 & \text{for } S_2,\ S_4 \end{cases} \tag{30}$$

Similarly, substituting (6) into (29), the ZV-on conditions of the switches on port 2 are expressed as

$$\begin{cases} \cos(\varphi_{23}\pi - D_2\pi/2) > k_2 & \text{for } S_5,\ S_7 \\ \cos(\varphi_{23}\pi + D_2\pi/2) > k_2 & \text{for } S_6,\ S_8 \end{cases} \tag{31}$$

Meanwhile, since i_{r3} is always in a phase of v_{EF} in this state, the ZC on is always achieved and independent of the topology parameters for all the switches on port 3.

State 2: when $k_1 < 1$, $k_2 > 1$,${G_{13}}^* > \sqrt{1-{k_1}^2}$ and ${G_{23}}^* \le \sqrt{1-{k_2}^2}$ or $k_1 \ge 1$, $k_2 < 1$ and ${G_{23}}^* \le \sqrt{1-{k_2}^2}$. The optimization result is expressed as

$$\begin{cases} {D_1}^* = 0 \\ {D_2}^* = \frac{2}{\pi}\arccos\left(\sqrt{{k_2}^2 + {G_2}^{*2}}\right) \\ {\varphi_{13}}^* = \frac{1}{\pi}\arcsin({G_1}^*) \\ {\varphi_{23}}^* = \frac{1}{\pi}\arctan(\frac{{G_2}^*}{k_2}) \end{cases} \tag{32}$$

The phasor diagram is shown in Figure 5b. In this state, the range of the voltage gain and transfer power between port 2 and port 3 is the same as that of state 1. According to the range of k_1, there are two cases of state 2: $k_1 < 1$ and $k_1 \ge 1$. They are represented by "I" and "II" in Figure 5b. In both cases, the relationship between the phase shifts of port 1 and ${G_{13}}^*$ is the same. The modulation of port 1 is simplified to SPS modulation, while there are some differences in the physical interpretation of the two cases.

(1) Case I ($k_1 < 1$): As ${G_{13}}^*$ increases, D_1 reduces to 0, and the magnitude of v_{ABf} increases to the maximum value v_{ABf,I_max}. Since the smaller the phase difference between i_{r1} and v_{EF}, the smaller the reactive power component and the RMS value of the transformer current. As ${G_{13}}^*$ continues to increase, the magnitude of v_{ABf} remains at v_{ABf,I_max} to minimize the phase difference between i_{r1} and v_{EF}. On this basis, the transfer power is only controlled by φ_{13}.

(2) Case II ($k_1 \geq 1$): The magnitude of v_{ABf} is always smaller than that of v_{EFf} in this case, thus there must be a phase difference between i_{r1f} and v_{EFf}. In order to minimize the phase difference between i_{r1} and v_{EF}, the magnitude of v_{ABf} remains at the maximum value v_{ABf,II_max} in the entire power range.

In both cases, the modulation of port 1 is simplified to SPS modulation. The corresponding soft-switching operation conditions have been analyzed in detail in [15]. The ZV-on condition of port 1 is expressed as

$$\cos(\varphi_{13}\pi) > k_1 \tag{33}$$

The operation state of port 2 is the same as that of state 1, hence, the ZV-on condition of port 2 is the same as (31).

For port 3, since the transformer currents of port 1 and port 2 are not in phase, it is difficult to get the analytical solution of i_{r3}. Combing the analysis in [15], the ZV-on condition is $\theta_3 > \varphi_{13}$. θ_3 is the lagging angle between i_{r3} and v_{AB}.

State 3: when $k_1 < 1$, $k_2 < 1$, ${G_{13}}^* \leq \sqrt{1-{k_1}^2}$ and ${G_{23}}^* > \sqrt{1-{k_2}^2}$ or $k_1 < 1$, $k_2 \geq 1$ and ${G_{13}}^* \leq \sqrt{1-{k_1}^2}$, the optimization result is expressed as

$$\begin{cases} {D_1}^* = \frac{2}{\pi}\arccos\left(\sqrt{{k_1}^2+{G_1}^{*2}}\right) \\ {D_2}^* = 0 \\ {\varphi_{13}}^* = \frac{1}{\pi}\arctan(\frac{{G_1}^*}{k_1}) \\ {\varphi_{23}}^* = \frac{1}{\pi}\arcsin({G_2}^*) \end{cases} \tag{34}$$

The phasor diagram is shown in Figure 5c. In this state, the range of the voltage gain and transfer power between port 1 and port 3 is the same as that of state 1. According to the range of k_2, there are two cases of state 3: $k_2 < 1$ and $k_2 \geq 1$. They are represented by "I" and "II" in Figure 5c. The physical interpretation of the two cases is similar to that of state 2, thus no detailed description is given here.

The soft-switching performance of this state is similar to that of state 2. The ZV-on condition of port 1 is the same as (30). The ZV-on condition of port 3 is $\theta_3 > \varphi_{13}$. The ZV-on condition of port 2 is expressed as

$$\cos(\varphi_{23}\pi) > k_2 \tag{35}$$

State 4: when $k_1 < 1$, $k_2 < 1$, ${G_{13}}^* > \sqrt{1-{k_1}^2}$ and ${G_{23}}^* > \sqrt{1-{k_2}^2}$ or $k_1 \geq 1$ and $k_2 \geq 1$, the optimization result is expressed as

$$\begin{cases} {D_1}^* = 0 \\ {D_2}^* = 0 \\ {\varphi_{13}}^* = \frac{1}{\pi}\arcsin({G_1}^*) \\ {\varphi_{23}}^* = \frac{1}{\pi}\arcsin({G_2}^*) \end{cases} \tag{36}$$

The phasor diagram is shown in Figure 5d. In this state, according to the range of k_1 and k_2, there are two cases of state 4. In both cases, the modulation strategies of port 1 and port 2 are simplified to SPS modulation.

(1) Case I ($k_1 < 1$ and $k_2 < 1$): As ${G_{13}}^*$ and ${G_{23}}^*$ increase, both D_1 and D_2 reduce to 0. The magnitude of v_{ABf} and v_{CDf} increases to the maximum value $v_{ABf,I\_max,}$ and v_{CDf,I_max}.

In order to reduce the RMS value of the transformer current, the magnitude of v_{ABf} remains at $v_{ABf,I\_max,}$ and the magnitude of v_{CDf} remains at v_{CDf,I_max}, as $G_{13}{}^{*}$ continues to increase.

(2) Case II ($k_1 \geq 1$ and $k_2 \geq 1$): The magnitude of v_{ABf} and v_{CDf} are smaller than that of v_{EFf}. Similarly, to minimize the RMS value of the transformer current, the magnitude of v_{ABf} and v_{CDf} respectively remains at the maximum value $v_{ABf,II\_max,}$ and v_{CDf,II_max} in the entire power range.

In this state, the modulation strategies of port 1 and port 2 are both simplified to SPS modulation. The ZV-on condition of port 1 and port 2 are expressed as (33) and (35), respectively. The ZV-on condition of port 3 is $\theta_3 > \varphi_{13}$.

In order to verify the performance of the optimized multi-phase-shift modulation, the RMS value of the transformer current of the optimized modulation is contrasted with that of the traditional SPS modulation. It is obtained from (25), (32), (34), and (36) that the main difference between the proposed modulation and the SPS modulation lies in the range of $k_1 < 1$ and $k_2 < 1$. Taking port 1 as an example, the RMS values of the transformer current of the two modulations under $k_1 < 1$ are compared. The internal phase-shift angles of the three ports are all 0 under the SPS modulation, and the external phase-shift angles satisfy

$$\varphi_{13}{}^{*} = \frac{1}{\pi}\arcsin(G_1{}^{*}),\ \varphi_{23}{}^{*} = \frac{1}{\pi}\arcsin(G_2{}^{*}) \tag{37}$$

The expressions (25), (32), and (36) are substituted into (16). The corresponding parameters are shown in Table 1 and k_1 is set to 0.6 and 0.8. The distribution curves of $I_{r1,rms}$ as a function of the transfer power $G_{13}{}^{*}$ of the two modulation strategies are drawn in Figure 6. It can be seen that the $I_{r1,rms}$ of the proposed strategy are significantly smaller than that of SPS modulation. In particular, as the voltage gain decreases, the advantage of the proposed modulation to reduce the RMS value of the transformer current is more obvious.

Table 1. Parameters of experimental platform.

Parameter	Value
v_1, v_2	60–150 V
v_3	100 V
f_s	50 kHz
n_1: n_2: n_3	1:1:1
L_{r1}, L_{r2}	209 μH
C_{r1}, C_{r2}	53 nF
L_{k3}	101 μH
C_{r3}	100 nF
Power switch (SiC JFETs)	650 V/50 A

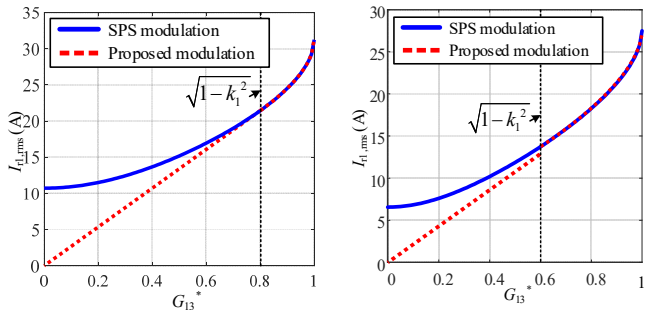

(**a**) (**b**)

Figure 6. Curves of RMS transformer current as a function of transfer power under different modulations. (**a**) k_1 = 0.6, (**b**) k_1 = 0.8.

According to the above analysis, the proposed modulation realizes the global optimized control of the converter, as compared to the SPS modulation. The optimized

modulation significantly reduces the RMS transformer current and the power loss. The converter efficiency is accordingly increased in the entire range of the voltage and transfer power.

4. Experimental Results and Analysis

The proposed three-port converter and optimized modulation are verified by the built experimental platform shown in Figure 7a. The modular approach is used to build the experimental platform. We have built some general half-bridge modules with the SiC power switches. The voltage rating of the switches is 650 V. Based on these modules, it is convenient to make up various dc-dc or dc-ac converters. Combining with the schematic of the proposed converter shown in Figure 1, we use six modules to make up the proposed three-port converter in this experiment. Then combining with (4), (8), and (9) the parameters of the resonant tank of port 1 and port 2 are designed according to the requirements of the transmission power level. Combining with (4), (12) and the switching frequency f_s, the parameters of the resonant tank of port 3 are designed. The input inductors and bus capacitors of port 1 and port 2 are designed according to the ripple requirements of the input current and the bus voltage. In addition, three dc voltage sources and three resistors are connected in parallel to the three ports, respectively, so that the power can be transferred among the three ports under the bi-direction. The parameters of the experimental platform are listed in Table 1. In order to verify the availability of the proposed modulation when the voltage gain varies in a wide range, the voltages on port 1 and 2 vary from 60 V to 150 V. In addition, to decrease the capacitance and rated voltage of the resonant capacitor used on port 3, an inductor is connected in series in the resonant tank. The total value of the leakage inductance of the transformer on port 3 and the external inductance is 101 μH. The three components construct the resonant tank with the resonant frequency of 50 kHz, which is equal to the switching frequency to realize the power decoupling. All experiments are performed under open-loop conditions. The control is implemented based on DSP + FPGA platform. The specific type of the used DSP and FPGA are TMS320F28377 and Cyclone IV, respectively. First, according to the range of voltage gain and transfer power, the operating state of the converter is selected. On this basis, the control variables are calculated, combined with (25), (32), (34), and (36). The above works are completed by DSP. Then, the calculations of DSP are transferred to FPGA and the driving signals of the switches are generated by FPGA. The block of the control configuration is shown in Figure 7b.

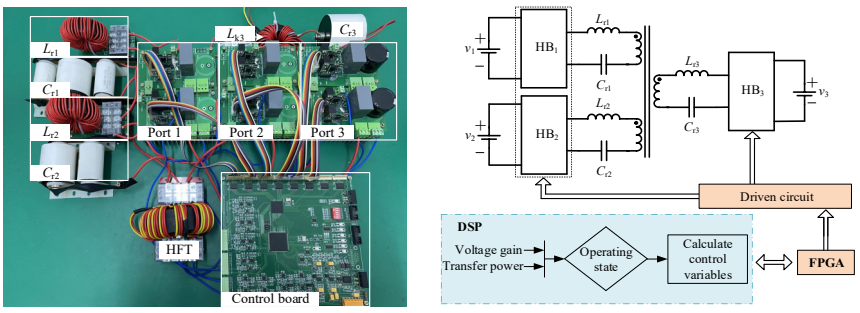

(**a**) (**b**)

Figure 7. Experimental platform. (**a**) Photograph, (**b**) Control configuration.

According to power flowing direction, there are three types of operation modes, namely the forward mode, backward mode, and hybrid mode. In order to verify the performance of the power decoupling and the optimized modulation in the entire power range, the experimental results of various operation modes are all tested and analyzed separately below. As a comparison, the corresponding experimental results of the conventional TAB resonant converter without the decoupling resonant tank are also tested and shown here.

First, the performance of decoupling of both port 1 and port 2 operating in the forward mode is verified and compared with that of the conventional converter. In order to observe the performance of the power decoupling, the transfer power of port 2 remained constant and that of port 1 is stepped at some time. The corresponding experimental results of the converter and the conventional converter and the proposed one are shown in Figure 8. From Figure 8a, in the conventional converter, when i_1 step change occurs, the current of port 2 i_2 varies accordingly.

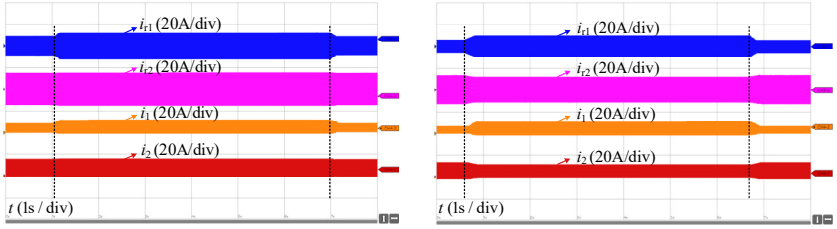

(**a**) (**b**)

Figure 8. Experimental results of power decoupling in the forward mode. (**a**) TAB converter without decoupling tank, (**b**) Proposed converter.

This clearly reveals the power coupling problem. From Figure 8b, in the proposed converter, i_2 keeps constant during the transient process, that is, the power coupling between port 1 and port 2 is eliminated.

In the following, the global optimal modulation in all states is tested and compared with the SPS modulation. In state 1, the input voltages of port 1 and port 2 are set as 120 V and 140 V. k_1 and k_2 are accordingly 0.83 and 0.71. The corresponding experimental waveforms of state 1 with P_{13} = 800 W and P_{23} = 1 kW are shown in Figure 9. Figure 9a shows the experimental results of the optimized modulation. D_1, D_2, φ_{13} and φ_{23} calculated by the optimal conditions in (25) are 0.15, 0.33, 0.16, and 0.19, respectively. i_{r1}, $i_{r2,}$ and i_{r3} are all in a phase of v_{EF}. Hence, the converter operates at the minimum RMS value of the transformer current. In contrast, the experimental results of the SPS modulation under the same transfer power are shown in Figure 9b. There is a phase difference between i_{r1}, i_{r2}, $i_{r3,}$ and v_{EF}. The RMS value of the transformer current under the SPS modulation is greater than that of the optimized modulation. The experimental results verify under the same transfer power, the optimized modulation effectively reduces the RMS value of the transformer current, thereby reducing the power loss of the converter, compared with the SPS modulation. In addition, the power switching transition types are marked in the corresponding experimental results. All power switches of the three ports realize the soft-switching under the proposed modulation.

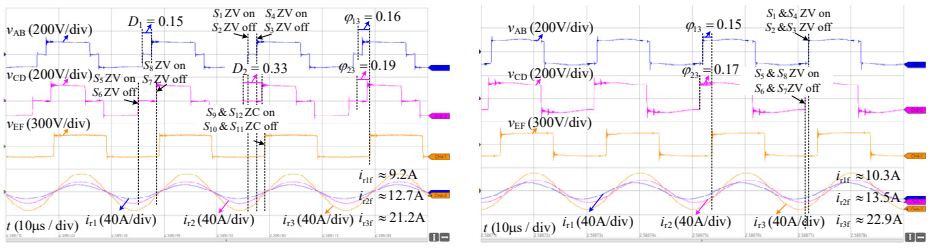

(**a**) (**b**)

Figure 9. Experimental results of state 1 in the forward mode. (**a**) Optimized modulation, (**b**) SPS modulation.

In state 2, there are two cases according to the range of k_1. First, the performance of the optimized modulation in the case of $k_1 < 1$ is tested. The transfer power of port 1 is set as 1kW. Figure 10a,b show the experimental results of the optimized modulation and those of the SPS modulation, respectively. D_1, D_2, φ_{13}, and φ_{23} calculated by the optimal

conditions in (27) are 0, 0.33, 0.2, and 0.19, respectively. It can be seen that, under the proposed modulation, port 2 operates at the unity power factor. The rms value of i_{r2} of the optimized modulation is smaller than that of the SPS modulation. For port 1, as the transfer power increases, D_1 reduces to 0 and port 1 operates with the maximum RMS value of v_{AB}. The modulation of port 1 is simplified to SPS modulation. Hence, the overall power loss and the RMS value of the transformer current of the optimized modulation are reduced compared with the SPS modulation.

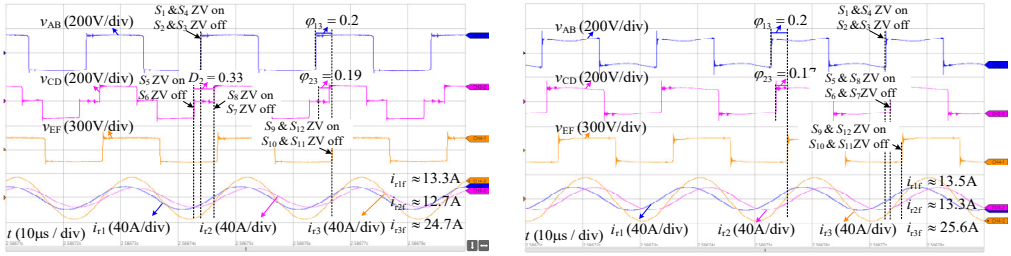

(**a**) (**b**)

Figure 10. Experimental results with k1 < 1 of state 2 in the forward mode. (**a**) Optimized modulation, (**b**) SPS modulation.

In the case of $k_1 > 1$, the voltage of port 1 and port 2 are 60 V and 140 V, and k_1 and k_2 are 1.67 and 0.71, accordingly. The transfer power of port 1 and port 2 is 500 W and 1 kW, respectively. D_1, D_2, φ_{13}, and φ_{23} calculated by the optimal conditions in (27) are 0, 0.33, 0.20, and 0.19, respectively. In this case, the magnitude of v_{AB} is always smaller than v_{EF}, thus the modulation of port 1 is also simplified to the SPS modulation to minimise the RMS value of i_{r1}. The corresponding experimental waveforms of the two modulations are shown in Figure 11. It can be seen that i_{r2} is in a phase of v_{EF} of the optimized modulation. The RMS value of i_{r2} and i_{r3} of the optimized modulation are smaller than those of the SPS modulation. Since the topologies of port 1 and port 2 are exactly the same, the experimental results of state 3 are similar to those of state 2. They are not shown here.

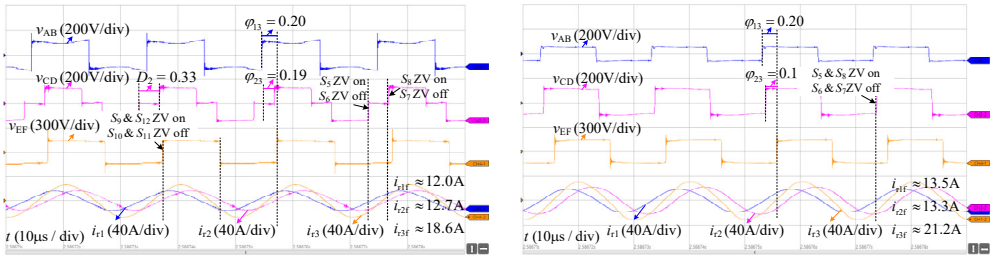

(**a**) (**b**)

Figure 11. Experimental results with k1 > 1 of state 2 in the forward mode. (**a**) Optimized modulation, (**b**) SPS modulation.

The experimental waveforms of state 4 of the optimal modulation are shown in Figure 12. The input voltage of port 1 and port 2 is 60 V and 80 V, and k_1 and k_2 are 1.67 and 1.25, accordingly. Since k_1 and k_2 are both greater than 1 in this state, the RMS value of the transformer current is minimized when the RMS value of v_{AB} and v_{CD} is the maximum. Hence, the optimized modulation is simplified into SPS modulation.

The above experimental results show that the RMS value of the transformer current under the optimized modulation is effectively reduced compared with the SPS modulation in the entire power range. Hence, the power loss of the converter is reduced.

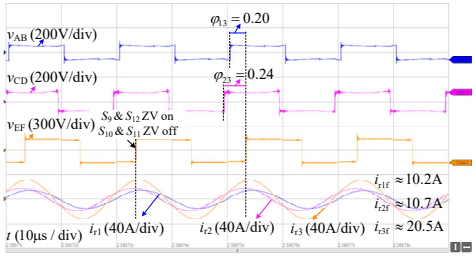

Figure 12. Experimental results of state 4 in the forward mode.

Then, the effectiveness of the power decoupling and the optimized modulation of both port 1 and port 2 operating at the backward mode are tested. Figure 13a shows the experimental results when the desired i_2 remains constant while i_1 is suddenly stepped. From Figure 13a, when i_1 is suddenly stepped, the actual i_2 remains constant. It means the proposed converter realizes the power decoupling in this case. Figure 13b shows the experimental results of the conventional TAB converter under the same conditions. From Figure 13b, i_2 varies when i_1 is stepped. Next, take state 1 as an example to test the optimized modulation. The steady-state waveforms are shown in Figure 14. Both port 1 and port 2 operate at the minimum transformer current and the RMS value of the transformer current is effectively reduced compared with the SPS modulation.

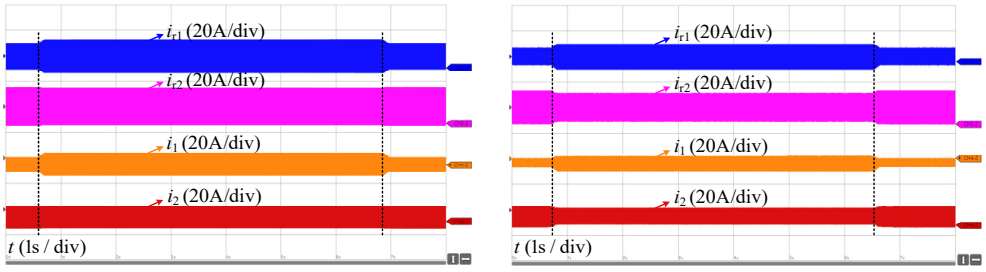

Figure 13. Experimental results in the backward mode. (**a**) Proposed converter, (**b**) TAB resonant converter without decoupling tank.

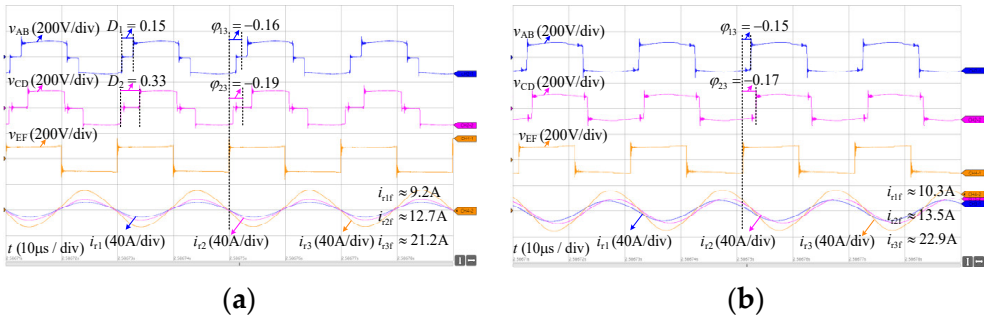

Figure 14. Experimental results of proposed converter in the backward mode. (**a**) Optimized modulation, (**b**) SPS modulation.

Similarly, the dynamic waveforms of port 1 operate in the forward mode and port 2 operating in the backward mode are shown in Figure 15. The corresponding steady-state waveforms under the optimized modulation are shown in Figure 16. These experimental results verify the converter eliminates the power coupling between port 1 and port 2 and reduces the RMS value of the transformer current under the hybrid mode.

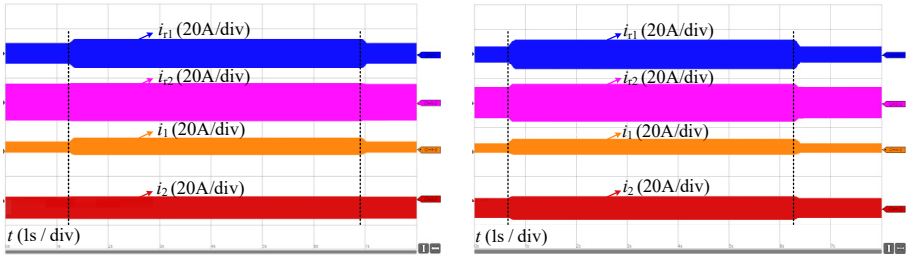

Figure 15. Experimental results in hybrid mode. (**a**) Proposed converter, (**b**) TAB resonant converter without decoupling tank.

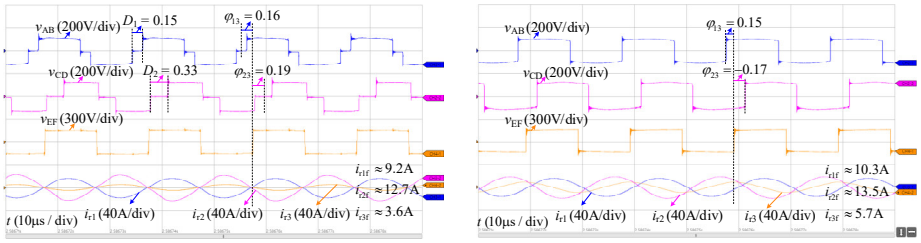

Figure 16. Experimental results of optimized modulation in hybrid mode. (**a**) Optimized modulation, (**b**) SPS modulation.

From the above experimental results, the proposed topology realizes the power decoupling, and the proposed modulation also significantly reduces the transformer current, in the entire power range and various operation modes.

Finally, take both port 1 and port 2 operating at the forward mode as an example to test the efficiency of the proposed converter under the proposed modulation and SPS modulation. The efficiency is tested and compared in the different states. The efficiency curves in the state of $k_1 < 1$ and $k_2 < 1$ are shown in Figure 17a. The efficiency curves in the state of $k_1 > 1$ and $k_2 < 1$ are shown in Figure 17b. It can be seen that the efficiency is all over 88% in the different states. Compared with the SPS modulation, the efficiency of the optimized modulation is effectively increased in a wide range of the transfer power and the voltage gain.

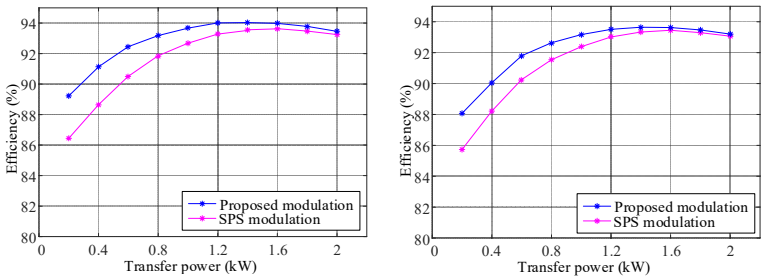

Figure 17. Efficiency curves of proposed converter under various modulations. (**a**) $k_1 < 1$ and $k_2 < 1$, (**b**) $k_1 > 1$ and $k_2 < 1$.

5. Conclusions

A TAB resonant dc-dc converter and hardware power decoupling method are proposed in this paper. By setting a resonant tank at the common port, the power coupling between the two separate ports is eliminated easily and any other power decoupling control is added. The proposed global optimization multi-phase-shift modulation significantly

reduces the RMS value of the transformer current in the entire power and voltage range. The power loss of the converter is accordingly reduced compared with the general SPS modulation. The proposed topology and optimized modulation simplify the control loop and improve the efficiency of the TAB converter and accordingly further enhance its practicability. In the future, the small-signal model of the proposed TAB resonant dc-dc converter will be established. Meanwhile, the closed-loop control strategy will be studied in-depth, based on the modulation proposed in this paper. Thus, the independent and precise control of the transfer power of the proposed converter is realized.

Author Contributions: Conceptualization, F.W. and K.W.; methodology, F.W.; software, J.S.; validation, K.W.; formal analysis, F.W. and K.W.; investigation, J.S.; writing—original draft preparation, K.W.; writing—review and editing, F.W. All authors have read and agreed to the published version of the manuscript.

Funding: This research was funded by the project of Science Foundation of Heilongjiang Province, grant number LH2021E066 and the Fundamental Research Funds for the Central Universities, grant number HIT.NSRIF202227.

Institutional Review Board Statement: Not applicable.

Informed Consent Statement: Not applicable.

Data Availability Statement: Not applicable.

Conflicts of Interest: The authors declare no conflict of interest.

References

1. Neira, S.; Pereda, J.; Rojas, F. Three-port full-bridge bidirectional converter for hybrid DC/DC/AC systems. *IEEE Trans. Power Electron.* **2020**, *35*, 13077–13084. [CrossRef]
2. Wang, H.; Blaabjerg, F. Reliability of capacitors for dc-link applications in power electronic converters—An overview. *IEEE Trans. Ind. Electron.* **2014**, *50*, 3569–3578. [CrossRef]
3. Vazquez, S.; Lukic, S.M.; Galvan, E.; Franquelo, L.G.; Carrasco, J.M. Energy storage systems for transport and grid applications. *IEEE Trans. Ind. Electron.* **2010**, *57*, 3881–3895. [CrossRef]
4. Pereira, T.; Hoffmann, F.; Zhu, R.; Liserre, M. A comprehensive assessment of multiwinding transformer-based dc–dc converters. *IEEE Trans. Power Electron.* **2021**, *36*, 10020–10036. [CrossRef]
5. Oluwasogo, E.S.; Cha, H. Self-current sharing in dual-transformer-based triple-port active bridge dc–dc converter with reduced device count. *IEEE Trans. Power Electron.* **2021**, *36*, 5290–5301. [CrossRef]
6. Jakka, V.N.S.R.; Shukla, A.; Demetriades, G.D. Dual-transformer-based asymmetrical triple-port active bridge (DT-ATAB) isolated dc–dc converter. *IEEE Trans. Ind. Electron.* **2017**, *64*, 4549–4560. [CrossRef]
7. Lee, J.Y.; Jung, J.H. Modified Three-Port DAB Converter Employing Voltage Balancing Capability for Bipolar DC Distribution System. *IEEE Trans. Ind. Electron.* **2022**, *69*, 6710–6721. [CrossRef]
8. Costa, L.F.; Buticchi, G.; Liserre, M. Optimum design of a multiple-active-bridge dc–dc converter for smart transformer. *IEEE Trans. Power Electron.* **2018**, *33*, 10112–10121. [CrossRef]
9. Nakagawa, S.; Arai, J.; Kasashima, R.; Nishimoto, K.; Kado, Y.; Wada, K. Dynamic performance of triple-active bridge converter rated at 400 V, 10 kW, and 20 kHz. In Proceedings of the 2017 IEEE 3rd International Future Energy Electronics Conference and ECCE Asia, Kaohsiung, Taiwan, 3–7 June 2017; pp. 1090–1094.
10. Hou, N.; Li, Y.W. Overview and comparison of modulation and control strategies for a nonresonant single-phase dual-active-bridge dc–dc converter. *IEEE Trans. Power Electron.* **2020**, *35*, 3148–3172. [CrossRef]
11. Rodríguez, A.; Vázquez, A.; Lamar, D.G.; Hernando, M.M.; Sebastián, J. Different purpose design strategies and techniques to improve the performance of a dual active bridge with phase-shift control. *IEEE Trans. Power Electron.* **2015**, *30*, 790–804. [CrossRef]
12. Bai, H.; Mi, C. Eliminate reactive power and increase system efficiency of isolated bidirectional dual-active-bridge dc–dc converters using novel dual-phase-shift control. *IEEE Trans. Power Electron.* **2008**, *23*, 2905–2914. [CrossRef]
13. Krismer, F.; Kolar, J.W. Efficiency-optimized high-current dual active bridge converter for automotive applications. *IEEE Trans. Ind. Electron.* **2012**, *59*, 2745–2760. [CrossRef]
14. Wu, F.; Feng, F.; Gooi, H.B. Cooperative Triple-Phase-Shift Control for Isolated DAB DC–DC Converter to Improve Current Characteristics. *IEEE Trans. Ind. Electron.* **2019**, *66*, 7022–7031. [CrossRef]
15. Bai, C.; Han, B.; Kwon, B.; Kim, M. Highly efficient bidirectional series-resonant dc/dc converter over wide range of battery voltages. *IEEE Trans. Power Electron.* **2020**, *35*, 3636–3650. [CrossRef]
16. Corradini, L.; Seltzer, D.; Bloomquist, D.; Zane, R.; Maksimović, D.; Jacobson, B. Minimum current operation of bidirectional dual-bridge series resonant dc/dc converters. *IEEE Trans. Power Electron.* **2012**, *27*, 3266–3276. [CrossRef]

17. Wu, F.; Fan, S.; Li, X.; Luo, S. Bidirectional buck–boost current-fed isolated dc–dc converter and its modulation. *IEEE Trans. Power Electron.* **2020**, *35*, 5506–5516. [CrossRef]
18. Krishnaswami, H.; Mohan, N. Three-port series-resonant dc–dc converter to interface renewable energy sources with bidirectional load and energy storage ports. *IEEE Trans. Power Electron.* **2009**, *24*, 2289–2297. [CrossRef]
19. Wang, P.; Lu, X.; Wang, W.; Xu, D. Hardware decoupling and autonomous control of series-resonance-based three-port converters in dc microgrids. *IEEE Trans. Ind. Appl.* **2019**, *55*, 3901–3914. [CrossRef]
20. Xiangli, K.; Li, S.; Smedley, K.M. Decoupled pwm plus phase-shift control for a dual-half-bridge bidirectional dc–dc converter. *IEEE Trans. Power Electron.* **2018**, *33*, 7203–7213. [CrossRef]
21. Biswas, I.; Kastha, D.; Bajpai, P. Small signal modeling and decoupled controller design for a triple active bridge multiport dc–dc converter. *IEEE Trans. Power Electron.* **2021**, *36*, 1856–1869. [CrossRef]
22. Michon, M.; Duarte, J.L.; Hendrix, M.; Simoes, M.G. A three-port bi-directional converter for hybrid fuel cell systems. In Proceedings of the IEEE Power Electronics Specialists Conference (PESC'04), Aachen, Germany, 20–25 June 2004; pp. 4736–4742.
23. Duarte, J.L.; Hendrix, M.; Simoes, M.G. Three-Port Bidirectional Converter for Hybrid Fuel Cell Systems. *IEEE Trans. Power Electron.* **2007**, *22*, 480–487. [CrossRef]
24. Akagi, H.; Yamagishi, T.; Tan, N.M.L.; Kinouchi, S.; Miyazaki, Y.; Koyama, M. Power-loss breakdown of a 750-V 100-kW 20-kHz bidirectional isolated dc–dc converter using SiC-Mosfet/SBD dual modules. *IEEE Trans. Ind. Appl.* **2015**, *51*, 420–428. [CrossRef]
25. Peng, F.Z.; Li, H.; Su, G.; Lawler, J.S. A new ZVS bidirectional DC-DC converter for fuel cell and battery application. *IEEE Trans. Power Electron.* **2004**, *19*, 54–65. [CrossRef]